

# Electroweak box diagram contribution for pion and kaon decay from lattice QCD

Jun-Sik Yoo<sup>1,\*</sup>, Tanmoy Bhattacharya<sup>1,†</sup>, Rajan Gupta<sup>1,‡</sup>, Santanu Mondal<sup>2,§</sup> and Boram Yoon<sup>3,||</sup>

<sup>1</sup>Los Alamos National Laboratory, Theoretical Division T-2, Los Alamos, New Mexico 87545, USA

<sup>2</sup>ArcVision Technologies, 34 Mahatma Gandhi Road, Kolkata 700009, India

<sup>3</sup>NVIDIA Corporation, Santa Clara, California 95051, USA

 (Received 24 May 2023; accepted 20 July 2023; published 18 August 2023)

One of the sensitive probes of physics beyond the standard model is the test of the unitarity of the Cabbibo-Kobyashi-Maskawa matrix. Current analysis of the first row is based on  $|V_{ud}|$  from fifteen superallowed  $0^+ \rightarrow 0^+$  nuclear  $\beta$  decays and  $|V_{us}|$  from the kaon semileptonic decay,  $K \rightarrow \pi \ell \nu_\ell$ . Modeling the nuclear effects in the  $0^+ \rightarrow 0^+$  decays is a major source of uncertainty, which would be absent in neutron decays. To make neutron decay competitive requires improving the measurement of neutron lifetime and the axial charge, as well as the calculation of the radiative corrections (RC) to the decay. The largest uncertainty in these RCs comes from the nonperturbative part of the  $\gamma W$ -box diagram, and lattice QCD provides a first principle method for its evaluation. Our calculations, using lattice configurations generated with highly improved staggered quarks by the MILC Collaboration, show that the analogous calculations for the pion and kaon decays are robust and give  $\Box_{\gamma W}^{VA}|_\pi = 2.810(26) \times 10^{-3}$  and  $\Box_{\gamma W}^{VA}|_{K^{0,SU(3)}} = 2.389(17) \times 10^{-3}$  in agreement with the previous analysis carried out by Feng *et al.* using a different discretization of the fermion action.

DOI: [10.1103/PhysRevD.108.034508](https://doi.org/10.1103/PhysRevD.108.034508)

## I. INTRODUCTION

In the intensity frontier, physics beyond the standard model (BSM) is probed by confronting accurate predictions of the standard model (SM) with precision experiments. Today, there are several tests showing roughly  $2-3\sigma$  deviations, one being the unitarity of the first row of the Cabbibo-Kobyashi-Maskawa (CKM) quark mixing matrix, which states that  $\Delta_{\text{CKM}} \equiv |V_{ud}|^2 + |V_{us}|^2 + |V_{ub}|^2 - 1$  should be zero. Current analyses show a  $\approx 3\sigma$  tension with the SM [1–4] using the most precise value of  $|V_{ud}|^2 = 0.94815(60)$  coming from the analysis of fifteen  $0^+ \rightarrow 0^+$  nuclear  $\beta$  decays [1,5], and  $|V_{us}|^2 = 0.04976(25)$  obtained from kaon semileptonic decays ( $K \rightarrow \pi \ell \nu_\ell$ ) along with the  $N_f = 2 + 1 + 1$ -flavor lattice result for  $f_+^K(0)$  [6]. The estimate of  $|V_{ub}|^2 \approx (2 \pm 0.4) \times 10^{-5}$  is too small to impact the unitarity test.

\*junsik@lanl.gov  
 †tanmoy@lanl.gov  
 ‡rajan@lanl.gov  
 §santanu.sinp@gmail.com  
 ||byoon@nvidia.com

Published by the American Physical Society under the terms of the [Creative Commons Attribution 4.0 International license](https://creativecommons.org/licenses/by/4.0/). Further distribution of this work must maintain attribution to the author(s) and the published article's title, journal citation, and DOI. Funded by SCOAP<sup>3</sup>.

A current analysis of the unitarity bound is shown in Fig. 1, with the errors from various sources in  $0^+ \rightarrow 0^+$  nuclear, nucleon, pion and kaon decays shown in Fig. 2. While the extraction of  $V_{ud}$  from superallowed  $0^+ \rightarrow 0^+$  nuclear decays is the best, it is still subject to significant uncertainty in the theoretical analysis of nuclear effects.

Theoretically, the neutron is a clean system, i.e., it has no uncertainty due to nuclear corrections. The largest theoretical uncertainty comes from the  $\gamma W$ -box diagram illustrated

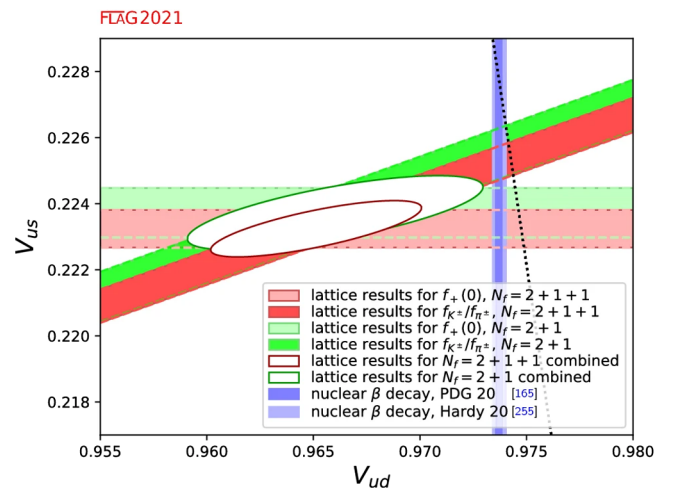


FIG. 1. Current status of the unitarity bound taken from the FLAG report 2021 [6].

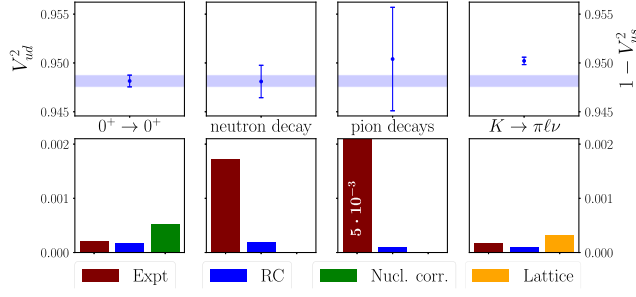


FIG. 2. The error budgets on the various extractions of  $|V_{ud}|^2$  and  $|V_{us}|^2$  to test the unitarity of the first row of the CKM matrix [1,7,8].

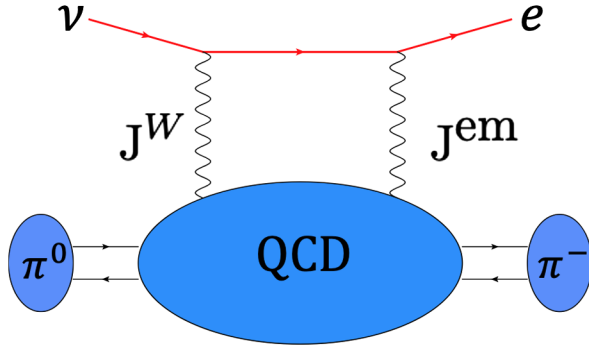


FIG. 3. The  $\gamma W$ -box diagram for RC to the pion decay.

in Fig. 3 for the pion as discussed in Refs. [9–11]. Lattice QCD can provide the least well-determined nonperturbative part of the  $\gamma W$ -box to reduce the uncertainty in the radiative corrections (RC) to neutron (and pion and kaon) decay. This, together with improvements in experiments measuring free neutron lifetime,  $\tau_n$ , and the axial charge,  $g_A$ , will make the extraction of  $|V_{ud}|^2$  from neutron decay competitive.

In this paper we present results for the pion and kaon (short for  $K \rightarrow \pi \ell \nu_\ell$ ) decay as we have not yet obtained a precise signal in the neutron correlation functions. Nevertheless, we provide a brief review of the status of the extraction of  $|V_{ud}|^2$  from neutron decay as it is the ultimate goal of this project. The analysis is carried out using the formula [4,12]

$$|V_{ud}|^2 = \left( \frac{G_\mu^2 m_e^5}{2\pi^3} f \right)^{-1} \frac{1}{\tau_n (1 + 3g_A^2)(1 + \text{RC})} = \frac{5099.3(3) \text{ s}}{\tau_n (1 + 3g_A^2)(1 + \text{RC})}, \quad (1)$$

where  $g_A$  is best obtained from the neutron  $\beta$  decay asymmetry parameter  $A$ ,  $G_\mu$  is the Fermi constant extracted from muon decays, and  $f = 1.6887(1)$  is a phase-space factor. With future measurements of the neutron lifetime  $\tau_n$  reaching an uncertainty of  $\Delta\tau_n \sim 0.1$  s, and of the ratio  $\lambda = g_A/g_V$  of the neutron axial and vector coupling reaching  $\Delta\lambda/|\lambda| \sim 0.01\%$ , the extraction of  $V_{ud}$  with accuracy comparable to  $0^+ \rightarrow 0^+$  superallowed  $\beta$  decay can be achieved

provided the uncertainty in the RC to neutron decay can be reduced.

The lattice methodology for the calculation of RC to pion, kaon and neutron decays is similar [10,11]. It requires the calculation of the  $\gamma W$ -box diagram, illustrated in Fig. 3 for the pion. From here on, we restrict the discussion to pion ( $\pi^+ \rightarrow \pi^0 \ell \nu_\ell$ ) and kaon to pion ( $K \rightarrow \pi \ell \nu_\ell$ ) semileptonic decays, for which the analog of Eq. (1) to extract  $|V_{ud}|^2$  and  $|V_{us}|^2$  are [1,13–15]

$$|V_{ud} f_+^\pi(0)|_{\pi\ell}^2 = \frac{64\pi^3 \Gamma_\pi}{G_\mu^2 M_\pi^5 I_\pi (1 + \delta)} \quad (2)$$

$$|V_{us} f_+^K(0)|_{K\ell}^2 = \frac{192\pi^3 \text{BR}(K\ell) \Gamma_K}{G_\mu^2 M_K^5 C_K^2 S_{\text{EW}} I_{K\ell} (1 + \delta_{\text{EM}}^{K\ell} + \delta_{\text{SU}(2)}^{K\ell})}, \quad (3)$$

where  $\Gamma_{\pi/K}$  are  $\pi$  and  $K$  decay rates,  $I_{\pi,K}$  are known kinematic factors,  $f_+^{\pi/K}$  are semileptonic form factors,  $C_K$  is a known normalization factor needed for kaon decay,  $S_{\text{EW}}$  is the short distance radiative correction, and the  $\delta_{\text{SU}(2)}^{K\ell}$  is the isospin breaking correction. The two (long distance) radiative corrections in which the uncertainty needs to be reduced are  $\delta$  for pion and  $\delta_{\text{EM}}^{K\ell}$  for kaon decay.

Looking ahead, the experimental uncertainty in pion decay needs to be reduced by a factor greater than 20, at which point it will become roughly equal to that in radiative corrections. PIONEER [16] is a next generation experiment aimed at measuring precisely the rare pion decay branching ratios. Its primary goal is to improve the measurement of the branching ratio of the semileptonic decay by up to a factor of ten, thus reducing the experimental uncertainty in  $|V_{ud}|^2$  by the same factor. At that point, as shown in Fig. 2, the experimental error in  $|V_{ud}|^2$  from pion decay will become comparable to that from  $0^+ \rightarrow 0^+$  superallowed nuclear decay, and also to the theory uncertainty.

In the determination of  $|V_{us}|$  from kaon  $\beta$  decay, the largest uncertainty comes from  $f_+^K(0)$  taken from lattice calculations [17]. Comparatively, the uncertainty in the radiative correction and experiments is already small [18].

This paper is organized as follows. The essential formulae needed to describe the calculation are summarized in the next Sec. II. The lattice setup, using ensembles generated by the MILC Collaboration [19,20], is specified in Sec. III. Error reduction methods used in the extraction of the hadronic tensor  $\mathcal{H}_{\mu\nu}^{VA}$  are described in Sec. IV. A comparison of results for the function  $\mathcal{M}_H(Q^2)$  defined in Eq. (8) and calculated using lattice QCD, with perturbation theory is made in Sec. V, and the extrapolation to the continuum limit is presented in Sec. VI. The final results and comparison to previous calculations are given in Sec. VII.

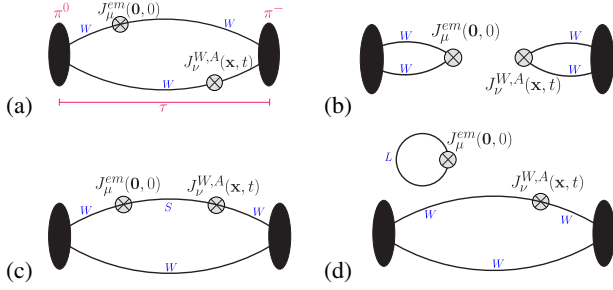


FIG. 4. The four quark-line diagrams that contribute to the pion  $\gamma W$ -box quantity  $\mathcal{H}_{\mu\nu}^{VA}(\vec{x}, t) = \langle \pi | T[J_{\mu}^{\text{em}}(x)J_{\nu}^{W,A}(0)] | \pi \rangle$  (right).

## II. ELECTROWEAK BOX DIAGRAM

Following the framework developed in [10,21], the electroweak box diagram [called the axial  $\gamma W$  diagram and shown in Fig. 3] is given by

$$\square_{\gamma W}^{VA} \Big|_H = \int_0^{+\infty} dQ^2 \int_{-Q}^Q dQ_0 \frac{1}{Q^4} \frac{1}{Q^2 + M_W^2} \times L^{\mu\nu}(Q^2, Q_0) T_{\mu\nu}^{VA}(Q^2, Q_0) \quad (4)$$

with  $H$  labeling the state,  $\pi$ ,  $K$  or  $N$ , under consideration, and  $M_W$  the  $W$  meson mass and  $M_H$  the hadron mass. Substituting in the known leptonic part  $L^{\mu\nu}(Q, Q_0)$  gives

$$\square_{\gamma W}^{VA} \Big|_H = -\frac{1}{F_+^H} \frac{\alpha_e}{\pi} \int_0^{\infty} dQ^2 \frac{m_W^2}{m_W^2 + Q^2} \times \int_{-\sqrt{Q^2}}^{\sqrt{Q^2}} \frac{dQ_0}{\pi} \frac{(Q^2 - Q_0^2)^{\frac{3}{2}}}{(Q^2)^2} \epsilon_{\mu\nu\alpha\beta} Q_{\alpha} P_{\beta} T_{\mu\nu}^{VA}. \quad (5)$$

The hadronic tensor  $T_{\mu\nu}^{VA}$  is given by

$$T_{\mu\nu}^{VA} = \frac{1}{2} \int d^4x e^{iQ \cdot x} \times \langle H_f(p) | T[J_{\mu}^{\text{em}}(\vec{x}, t) J_{\nu}^{W,A}(0, 0)] | H_i(p) \rangle, \quad (6)$$

where  $J_{\mu}^{\text{em}} = Z_V(\frac{2}{3}\bar{u}\gamma_{\mu}d - \frac{1}{3}\bar{d}\gamma_{\mu}d - \frac{1}{3}\bar{s}\gamma_{\mu}s)$  and  $J_{\mu}^{W,A} = Z_A\bar{u}\gamma_{\mu}\gamma_5 d$  are the renormalized currents with  $Z_V$  and  $Z_A$  calculated in Ref. [22].

Only one term,  $T_3$ , in the expansion  $T_{\mu\nu}^{VA} = i\epsilon_{\mu\nu\alpha\beta} q^{\alpha} p^{\beta} T_3 + \dots$  of the spin-independent part of  $T_{\mu\nu}^{VA}$  contributes [3,10]. Knowing  $T_3$  as a function of  $Q^2$ , the  $\gamma W$ -box correction, using the notation in Refs. [10,11], is given by

$$\square_{\gamma W}^{VA} = \frac{3\alpha_e}{2\pi} \int \frac{dQ^2}{Q^2} \frac{M_W^2}{M_W^2 + Q^2} \mathcal{M}_H(Q^2) \quad (7)$$

with

$$\begin{aligned} \mathcal{M}_H(Q^2) &= -\frac{1}{6} \frac{1}{F_+^H} \frac{\sqrt{Q^2}}{M_H} \int d^4x \omega(\vec{x}, t) \\ &\quad \times \epsilon_{\mu\nu\alpha 0} x_{\alpha} \mathcal{H}_{\mu\nu}^{VA}(\vec{x}, t), \\ \omega(t, \vec{x}) &= \int_{-\frac{\pi}{2}}^{\frac{\pi}{2}} \frac{\cos^3 \theta d\theta}{\pi} \frac{j_1(\sqrt{Q^2} |\vec{x}| \cos \theta)}{|\vec{x}|} \\ &\quad \times \cos(\sqrt{Q^2} t \sin \theta), \end{aligned}$$

$$\mathcal{H}_{\mu\nu}^{VA}(\vec{x}, t) = \langle H_f(p) | T[J_{\mu}^{\text{em}}(\vec{x}, t) J_{\nu}^{W,A}(0, 0)] | H_i(p) \rangle. \quad (8)$$

Here  $j_1$  in the weight function  $\omega(t, \vec{x})$  is the spherical Bessel function. The calculation of the hadronic part  $\mathcal{H}_{\mu\nu}^{VA}(\vec{x}, t)$  with the insertion of vector (V) and axial (A) currents gives rise to, in general, four types of Wick contractions shown by the quark-line diagrams in Fig. 4 for pion decay. It is a function of the separation  $\{\vec{x}, t\}$ , and on the lattice, the integral becomes a sum. As can be seen from Eq. (8),  $\mathcal{M}_H(Q^2)$  is however, available for all values of  $Q^2$ . One expects the signal in  $\mathcal{H}_{\mu\nu}^{VA}(\vec{x}, t)$  to fall off with  $\{\vec{x}, t\}$ , and in Fig. 5, we show that the integral saturates for  $R^2 \gtrsim 2 \text{ fm}^2$ . To be conservative and save computation time, we choose the integration volume to be larger than  $R^2 \sim 3.3 \text{ fm}^2$  on all the ensembles.

## III. LATTICE SETUP

The calculation has been performed using eight  $N_f = 2 + 1 + 1$  highly improved staggered quark (HISQ) ensembles generated by the MILC Collaboration [19,20], whose parameters are given in Table I, and shown in the  $\{a, M_{\pi}\}$  plane in Fig. 6. For comparison, we also show the parameters in the ‘‘Iwasaki’’ and ‘‘DSDR’’ variants of domain-wall fermions used in Ref. [10].

The correlation functions are constructed using Wilson-clover fermions, and the tuning of the light quark mass in

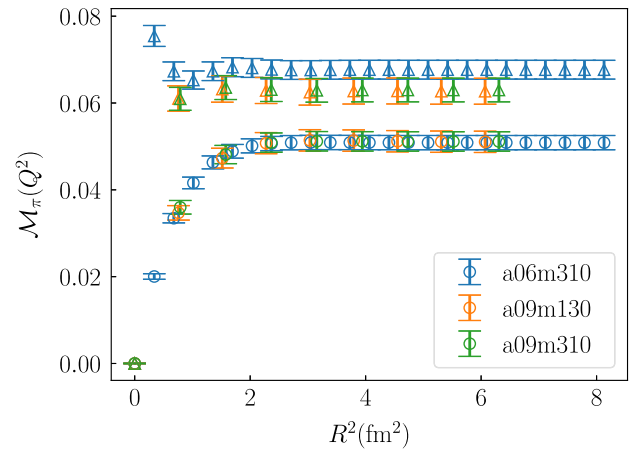


FIG. 5. The dependence of  $\mathcal{M}_{\pi}$  on  $R^2$  to check convergence. (See Sec. II for details.) Circles are used for  $Q^2 = 0.317 \text{ GeV}^2$  and triangles for  $Q^2 = 3.0 \text{ GeV}^2$  data.

TABLE I. Description of the eight HISQ ensembles generated by the MILC Collaboration [19,20] and used in this work. To increase the statistics, we create, on each configuration, 8 sublattices and in each make 256 measurements for diagram A and 64 for diagram C. The values of  $a$ ,  $M_\pi^{\text{sea}}$  and  $M_\pi^{\text{val}}$  are reproduced from Ref. [22].

Ensemble ID	$a(\text{fm})$	$\alpha_s$	$m_\pi^{\text{val}}(\text{MeV})$	$m_\pi^{\text{sea}}(\text{MeV})$	$L^3 \times T$	$m_\pi L$	$\tau/a$	$(R/a)^2$	$R^2(\text{fm}^2)$	$N_{\text{conf}}$
a06m310	0.0582(04)	0.2433	319.3(5)	319.3(5)	$48^3 \times 144$	4.52	62	1600	5.42	168
a09m130	0.0871(06)	0.2871	138.1(1.0)	128.2(1)	$64^3 \times 96$	3.90	40	800	6.07	45
a09m220	0.0872(07)	0.2873	225.9(1.8)	220.3(2)	$48^3 \times 96$	4.79	40	800	6.07	93
a09m310	0.0888(08)	0.2897	313.0(2.8)	312.7(6)	$32^3 \times 96$	4.51	40	800	6.31	156
a12m220	0.1184(09)	0.3348	227.9(1.9)	216.9(2)	$32^3 \times 64$	4.38	30	400	5.61	150
a12m220L	0.1189(09)	0.3348	227.6(1.7)	217.0(2)	$40^3 \times 64$	5.49	30	400	5.65	150
a12m310	0.1207(11)	0.3384	310.2(2.8)	305.3(4)	$24^3 \times 64$	4.55	30	400	5.83	179
a15m310	0.1510(20)	0.3881	320.6(4.3)	306.9(5)	$16^3 \times 48$	3.93	24	400	9.12	80

the isosymmetric limit is done by requiring  $M_\pi^{\text{valence}} = M_\pi^{\text{sea}}$  as described in Ref. [22] and their values are given in Table I. The strong coupling  $\alpha_s$  at each lattice ensemble was computed using fourth-order perturbative expression [23] with  $\Lambda_{\text{QCD}}^{n_f=4} = 292 \text{ MeV}$  taken from [24].

Of the four quark-line diagrams shown in Fig. 4, diagrams A and C are called “connected”. The “disconnected” diagram (B) does not contribute due to the  $\gamma_5$ -hermiticity property of the quark propagator, and diagram (D) vanishes in the  $SU(3)$  limit. This calculation has not been done at the  $SU(3)$  point, nevertheless we neglect diagram (D) assuming it is small. Under the same assumption, we also neglect contributions of the charm quark. To construct these correlation functions, quark propagators are generated using wall sources at two ends of a sublattice with separation  $\tau$  in time (see Table I). We label these quark lines by W. For the internal line S in

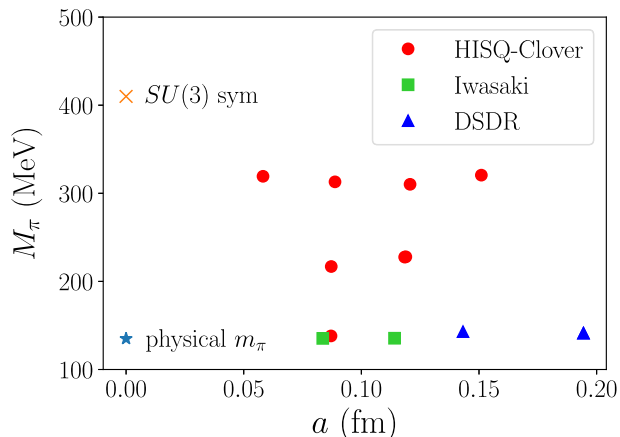


FIG. 6. The lattice spacing and pion mass of the eight ensembles (red circles) with  $2+1$ -flavors of Wilson-clover fermions analyzed in this study. The physical point (star) and  $SU(3)$  symmetric point (cross) are also shown. We also show the points for DSDR (triangle) and Iwasaki (square) actions that were used in Feng *et al.* [10,11].

diagram C, we solve for an additional propagator from the position of the vector current  $V_\mu$  placed on the middle time slice between the source and sink. This point is labeled  $\{\vec{x} = 0, t = 0\}$ . We choose 256 such points for diagram A and 64 for diagram C. Data are collected with the position of  $A_\mu$  varied within distance  $R^2$ , listed in Table I, from these points. On each configuration, we use 8 regions (sublattices) offset by  $N_T/8$  on which we repeat the calculation to further increase the statistics. With the current statistics, the errors in the data from the eight ensembles are comparable as shown later in Figs. 7 and 12. Since the total error budget for the box diagram is already dominated by the uncertainty in the renormalization constant  $Z_A$  as shown in Fig. 7, the current statistics are considered sufficient.

In Fig. 8, we show the result for  $\mathcal{M}_H$  and the  $\gamma W$ -box as a function of the separation  $\tau$  between the wall source and sink. Our data show no significant dependence on  $\tau > 2.4 \text{ fm}$ , at which separation only the ground state of the pseudoscalar mesons contributes to the calculation. To be conservative and because the signal in correlation functions for pseudoscalar mesons does not degrade with  $\tau$ , we chose to work with  $\tau$  in the range  $[3.48 \leq \tau \leq 3.63] \text{ fm}$  on all

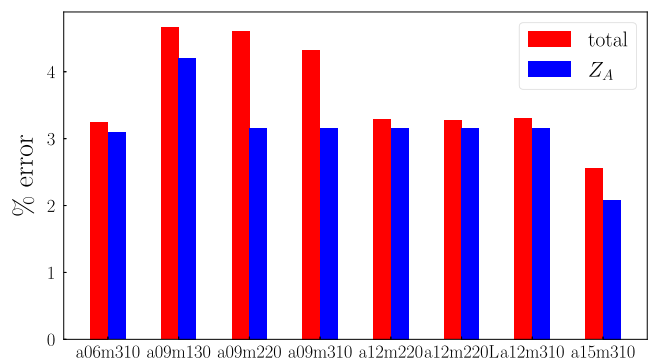


FIG. 7. Fractional error in the calculation of the box diagram for the pion on the eight ensembles. The total uncertainty (red bar) in the calculation is dominated by the uncertainty from the renormalization constant  $Z_A$  (blue bar).

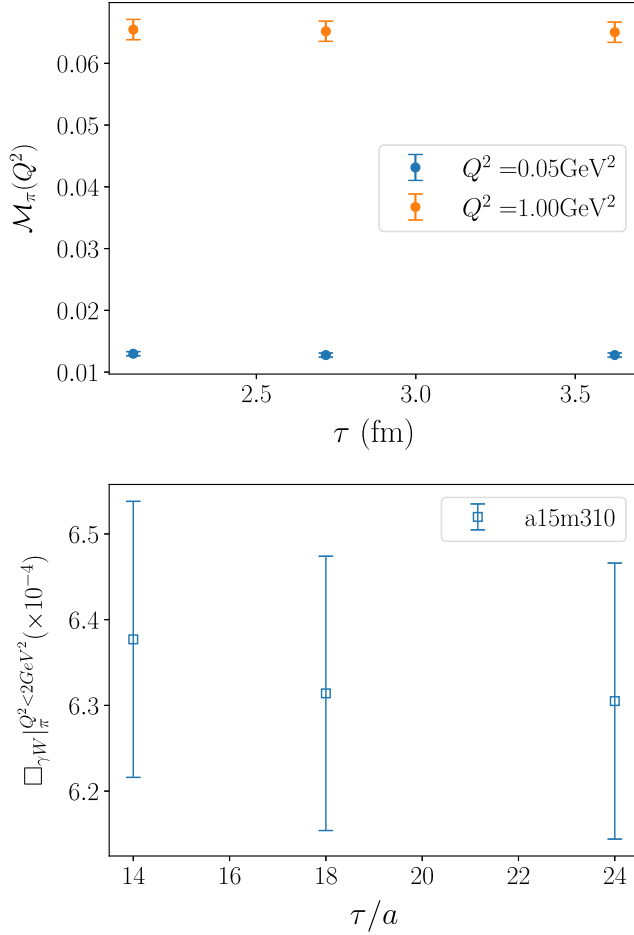


FIG. 8. The data for  $\mathcal{M}_\pi(Q^2)$  and the  $\gamma W$ -box contribution on the  $a15m310$  ensemble show no significant dependence on the source-sink separation  $\tau$ . We chose to perform all analyses in this paper with  $\tau$  in the range  $[3.48 \leq \tau \leq 3.63]$  fm.

ensembles. Note that this ability to choose  $\tau$  large enough to isolate the ground state is special to pseudoscalar mesons. For our target case of neutrons, the signal decays exponentially and excited state contamination may be a severe challenge [25]. As a result, even with much larger statistics, our ongoing calculations for neutrons have not yet yielded a statistically significant signal.

#### IV. ERROR REDUCTION IN THE EXTRACTION OF $\mathcal{H}_{\mu\nu}^{VA}$

The spectral decomposition of the two-point correlator of the pion is

$$\begin{aligned}
 C_{2\text{pt}}(\tau) &= C_{2\text{pt}}^{\text{fwd}}(\tau) + C_{2\text{pt}}^{\text{bkw}}(\tau) \\
 &= \sum_{\mathbf{x}} e^{-i\mathbf{p}\cdot\mathbf{x}} \langle J_\pi(\mathbf{x}, \tau) J_\pi^\dagger(0) \rangle \\
 &= \sum_i |\langle 0 | J_\pi | \pi_i(p) \rangle|^2 \frac{e^{-E_i(\mathbf{p})\tau} + e^{-E_i(\mathbf{p})(T-\tau)}}{2E_i(\mathbf{p})}, \quad (9)
 \end{aligned}$$

where  $i$  indexes the states. Statistics for  $C_{2\text{pt}}(\tau)$  are increased by averaging over forward and backward propagation. From here on, we truncate the sum over states to just the ground state since insertions of both currents,  $V_\mu$  and  $A_\mu$ , are made within the plateau region, i.e., far enough away from both source and sink time slices such that contributions of excited states are negligible.

The spectral decomposition of the hadronic tensor, limited to zero momentum neutron source and sink created using wall sources for quark propagators, and normalized by the 2-point function, is

$$\begin{aligned}
 R_{\mu\nu}^H(\tau, \vec{x}, t) &= \frac{C_{4\text{pt}}(\tau, \vec{x}, t)}{C_{2\text{pt}}^{\text{fwd}}(\tau)} \\
 &\stackrel{\tau \rightarrow 0}{=} \frac{2M_\pi \langle J_{\pi^0}(\tau/2) J_\mu^{\text{em}}(0, 0) J_\nu^{W,A}(\vec{x}, t) J_{\pi^-}(-\tau/2) \rangle}{|\langle 0 | J_\pi | \pi \rangle|^2 e^{-M_\pi \tau}}, \\
 &\stackrel{\tau \rightarrow 0}{=} \langle \pi^0(p) | T [J_\mu^{\text{em}}(0, 0) J_\nu^{W,A}(\vec{x}, t)] | \pi^-(p) \rangle / 2M_\pi \\
 &= \mathcal{H}_{\mu\nu} / 2M_\pi, \quad (10)
 \end{aligned}$$

where for the forward correlator,  $C_{2\text{pt}}^{\text{fwd}}(\tau)$ , one can use the fit or the data. These relations also apply for the kaon decay (short for  $K \rightarrow \pi \ell \nu_\ell$ ) as our calculation is done in the approximation of  $SU(3)$  symmetry.

The form factor  $F_+^H$  (matrix element) is obtained from the 3-point function,

$$F_+^H = \frac{\langle H(p') | J_\mu^V | H(p) \rangle}{(p + p')_{\mu=4}} = \frac{\sqrt{2} C_{3\text{pt}}(\tau)}{C_{2\text{pt}}^{\text{fwd}}(\tau)}, \quad (11)$$

for  $H = \pi$ . For  $H = K$ , the factor  $\sqrt{2}$  is absent. Thus, we can calculate the desired ratios

$$\frac{\mathcal{H}_{\mu\nu}^{VA}(\vec{x}, t)}{F_+^\pi} = 2M_\pi \frac{C_{4\text{pt}}(\tau, \vec{x}, t)}{\sqrt{2} C_{3\text{pt}}(\tau)}, \quad (12)$$

$$\frac{\mathcal{H}_{\mu\nu}^{VA}(\vec{x}, t)}{F_+^K} = 2M_K \frac{C_{4\text{pt}}(\tau, \vec{x}, t)}{C_{3\text{pt}}(\tau)}, \quad (13)$$

in two ways; first, using the left-hand side with  $F_+^\pi(0) = \sqrt{2}$  and  $F_+^K(0) = 1$ , where the factor  $\sqrt{2}$  comes from the normalization of the pion states. In the second method, we use the ratio of correlation functions in the right hand side of Eq. (13). As shown in Fig. 9, the errors in the 3- and 4-point functions are correlated and partially cancel in the second method, which is therefore used for the final results.

#### V. COMPARING LATTICE RESULTS FOR $\mathcal{M}_H(Q^2)$ WITH PERTURBATION THEORY

As mentioned in Sec. II,  $\mathcal{M}_H$  can be extracted at all values of  $Q^2$ . In practice, we choose sixty  $Q^2$  values that are the same on all eight ensembles with a higher density below  $Q^2 < 1 \text{ GeV}^2$ . Data at these 60 points are converted

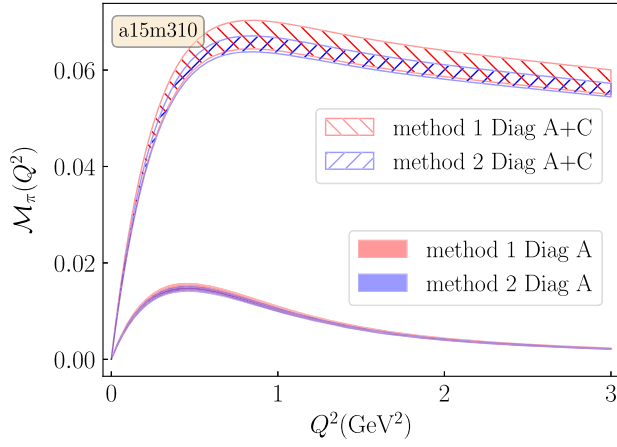


FIG. 9. Comparison of the signal in  $\mathcal{M}_\pi(Q^2)$  extracted using method 1 combining the ratio defined in Eq. (10) and  $F_\pi^\pm = \sqrt{2}$  (red), and using method 2, i.e., the ratio in Eq. (13) (blue). There is roughly a factor of two reduction in errors using Eq. (13) as can be deduced by comparing the blue and red bands.

into the smooth curves shown in Fig. 10 (top) using the cubic spline interpolator from scipy library [26]. Data show that as  $Q^2$  increases above 1 GeV<sup>2</sup>, the value of  $\mathcal{M}_H$  on coarser lattices decreases, indicating a dependence on the lattice spacing. Below  $Q^2 < 1$  GeV<sup>2</sup>, the trend reverses. The integrated box contributions for  $Q^2 < 2$  GeV<sup>2</sup> and their dependence on  $a$  and  $M_\pi^2$  is shown in Fig. 11.

To compare the  $\mathcal{M}_H(Q^2)$  from lattice and perturbation theory, we extrapolate the data to the continuum limit at  $M_\pi = 135$  MeV using a fit linear in  $\alpha_S a$  since the dependence on  $M_\pi$  is observed to be small (See Fig. 12). These fits, for all the ensembles and all  $Q^2$  values, have a  $p$ -value above 0.2. As shown in Fig. 10, this continuum limit data, represented by the gray solid line, roughly agrees with the perturbative result obtained using the operator product expansion [10,27,28] (gold line) for  $Q^2 > 2$  GeV<sup>2</sup>. Uncertainty in the perturbative result arises from the truncation of the series at the fourth-order and the neglected higher-twist (HT) contributions [10]. Since diagram (A) only has HT contributions, we use its full lattice value as an estimate of the HT uncertainty and show this by the dotted lines about the perturbative result.

## VI. CONTINUUM EXTRAPOLATION OF THE LATTICE DATA

The extrapolation of the  $\gamma W$ -box for  $Q^2 < Q_{\text{cut}}^2$  to the continuum limit  $a = 0$  and pseudoscalar mass  $M_\pi = M_\pi^{\text{phys}}$  for the pion, and  $M_\pi = M_K^{\text{SU}(3)}$  for the kaon is carried out keeping the lowest-order dependence on the pion mass,  $M_\pi^2$ , and on the lattice spacing,  $\alpha_S a$ ,

$$\square_{VA}^{Q^2 < Q_{\text{cut}}^2}(M_\pi, a) = c_0 + c_1 \alpha_S a + c_2 M_\pi^2. \quad (14)$$

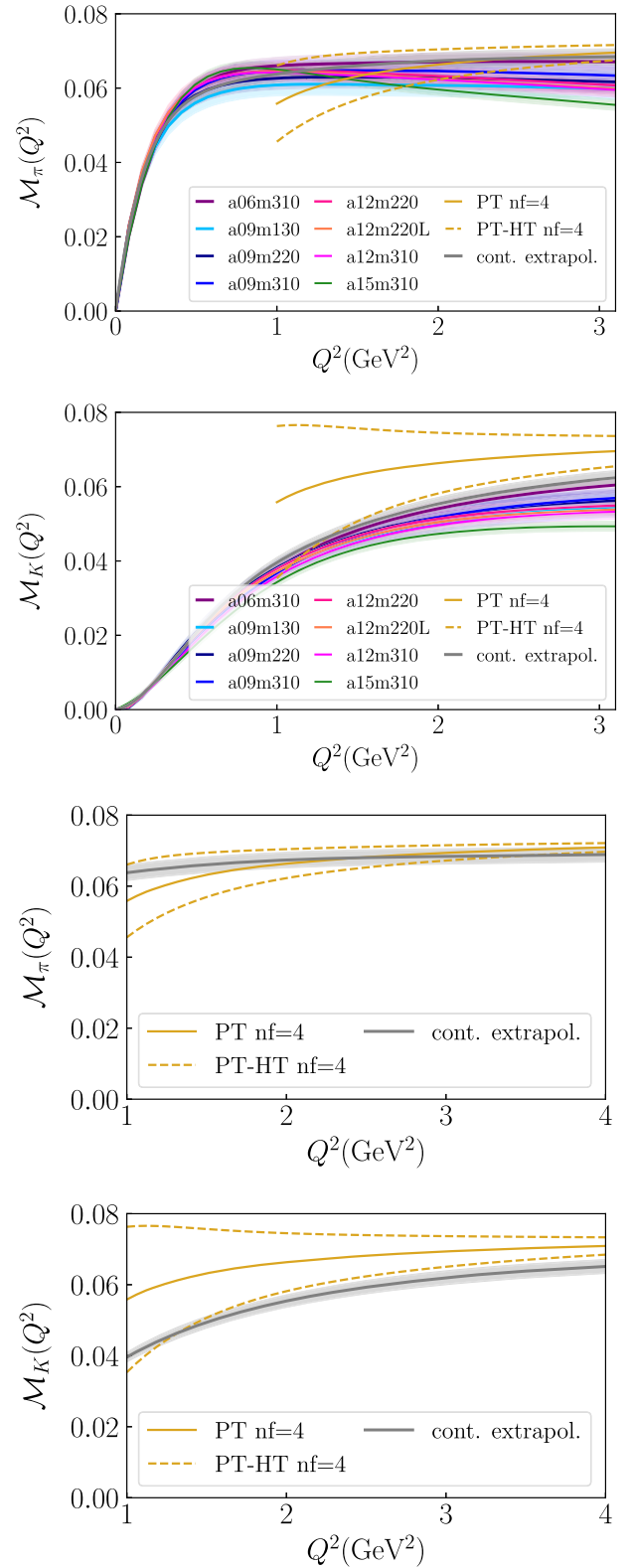


FIG. 10.  $\mathcal{M}_H(Q^2)$  for the pion and the kaon from the eight ensembles is shown in the top two panels. The bottom panels zoom in on the comparison between the continuum extrapolation using the 60  $Q^2$  values (gray band) and the gold line shows the perturbative result along with an uncertainty band reflecting higher-twist corrections.

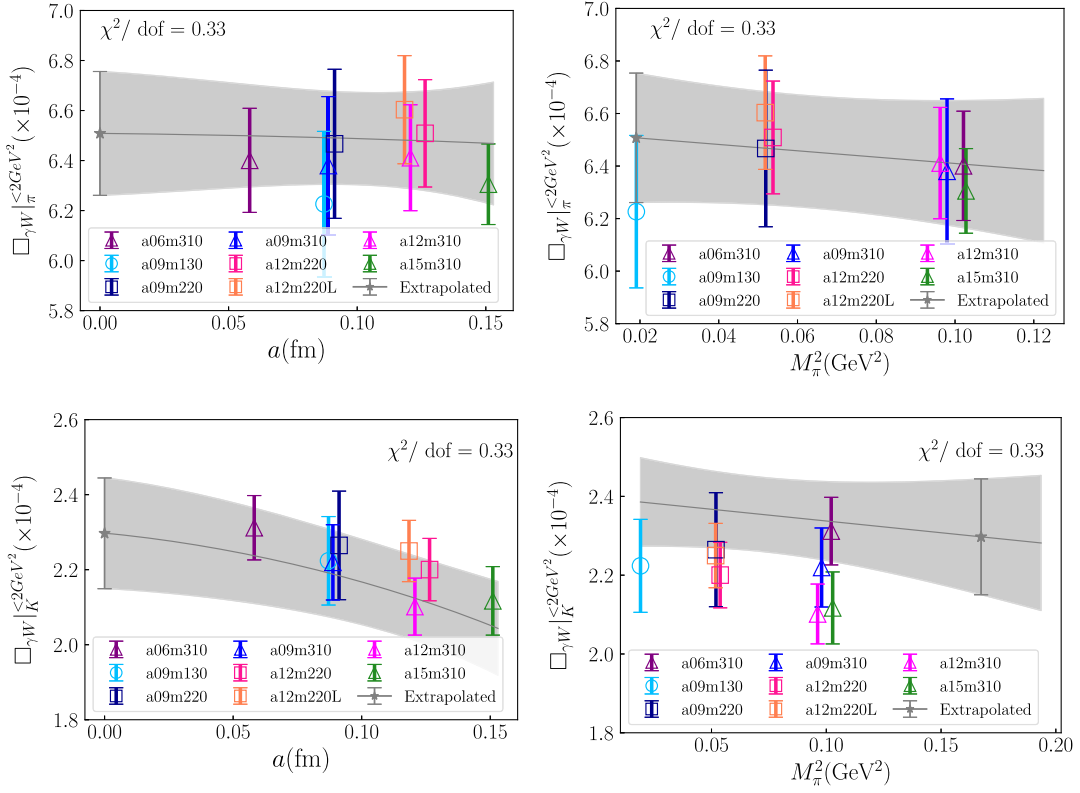


FIG. 11. The dependence of the  $\gamma W$ -box contribution for  $Q^2 \leq 2 \text{ GeV}^2$  for the pion (top) and kaon (bottom) decay on the lattice spacing  $a$  (left), and the pion mass ( $M_\pi^2$ ) (right). The symbols for the various ensembles are defined in the inset and in Table I. The physical point result given by the simultaneous fit in  $a$  and  $M_\pi^2$  (gray band) is shown by the gray star symbol. The result for the kaon is evaluated at the  $SU(3)$  symmetric point.

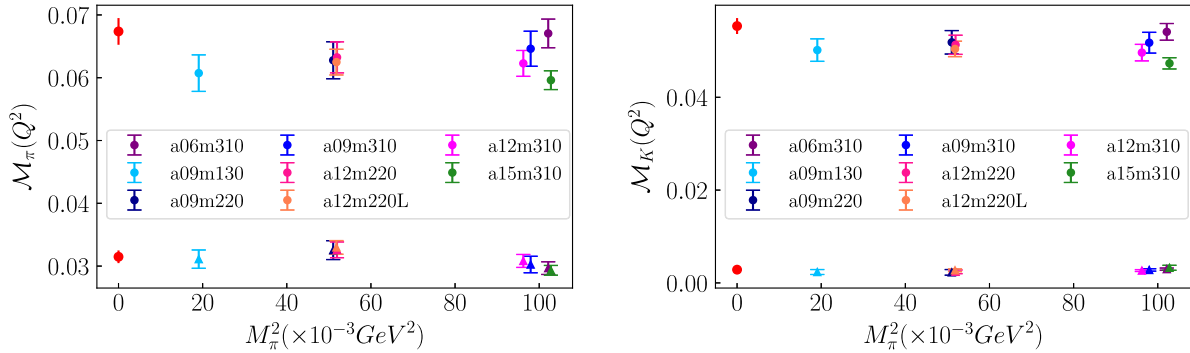


FIG. 12.  $\mathcal{M}_H(Q^2)$  for the pion (left) and kaon (right) at  $Q^2 = 0.133 \text{ GeV}^2$  (triangles),  $2.00 \text{ GeV}^2$  (circles). Ensembles are labeled by color. Data for  $\mathcal{M}_H(Q^2)$  do not show a significant dependence on  $M_\pi^2$ . The red points on the very left are the continuum extrapolated values using a fit linear in  $a\alpha_s$ , i.e., ignoring possible dependence on  $M_\pi^2$ .

This extrapolation is shown in (Fig. 11) and gives

$$\square_{\gamma W}^{\text{VA}}|_{\pi}^{Q^2 \leq 2 \text{ GeV}^2} = 0.651(25) \times 10^{-3}, \quad (15)$$

$$\square_{\gamma W}^{\text{VA}}|_{K}^{Q^2 \leq 2 \text{ GeV}^2} = 0.230(15) \times 10^{-3}, \quad (16)$$

Systematic uncertainties due to the chiral-continuum extrapolation are included in these estimates. We also estimated possible uncertainty in  $\mathcal{M}_H$  due to integration

using 52 discrete points in  $Q^2$  as the difference between using the trapezoid and Simpson methods and found it to be negligible. We assume finite volume effects are negligible since all the ensembles have  $M_\pi L \geq 3.9$ .

## VII. RESULTS FOR THE $\gamma W$ -BOX DIAGRAM AND COMPARISON TO EARLIER WORKS

The contribution above the energy cut at  $Q^2 = 2 \text{ GeV}^2$  is computed using the operator product expansion [10]

with the higher-twist uncertainty estimated using diagram A (See Fig. 4).

$$\square_{\gamma W}^{VA}|_{\pi,K}^{Q^2 > 2 \text{ GeV}^2} = 2.159(6)_{HO}(7)_{HT} \times 10^{-3}. \quad (17)$$

Combining Eq. (17) with Eq. (16) gives our results for the full box contribution,

$$\square_{\gamma W}^{VA}|_{\pi} = 2.810(26) \times 10^{-3}, \quad (18)$$

$$\square_{\gamma W}^{VA}|_{K^{0,SU(3)}} = 2.389(17) \times 10^{-3}, \quad (19)$$

which are in good agreement with those obtained by Feng *et al.* [10,11]:

$$\square_{\gamma W}^{VA}|_{\pi} = 2.830(11)(26) \times 10^{-3}, \quad (20)$$

$$\square_{\gamma W}^{VA}|_{K^{0,SU(3)}} = 2.437(44) \times 10^{-3}. \quad (21)$$

The difference in  $\square_{\gamma W}^{VA}|_{K^{0,SU(3)}}$  is  $1.02\sigma$ , but note that our value is determined with extrapolation in  $M_{\pi}^2$  to  $SU(3)$ -symmetric point, while the Feng *et al.* value, also called  $\square_{\gamma W}^{VA}|_{K^{0,SU(3)}}$ , was computed at the physical pion mass in all five ensembles, i.e., without extrapolation to  $M_K|_{SU(3)}$ .

The agreement between the two calculations provides an important consistency check as they are done at different values of  $\{a, M_{\pi}\}$  (see Fig. 6) and with different lattice actions. The largest uncertainty in the results presented in [10,11] comes from the systematic difference between DSDR and Iwasaki estimates, whereas in our calculation, as shown in Fig. 7, it comes from the renormalization constant  $Z_A$ , which is unity for domain-wall fermions.

Our data from the eight ensembles, all with the same action, provide a more controlled chiral-continuum extrapolation than in [10,11]. The data for the pion display no significant dependence on  $a$  or  $M_{\pi}^2$ . The data for the kaon in Fig. 11 shows  $\approx 10\%$  dependence on  $a$  but is flat with respect to  $M_{\pi}^2$ . A similar level of dependence on  $a$  was found in the Iwasaki action data in Ref. [11].

To conclude, taking the two calculations together increases our confidence that lattice QCD calculations of the nonperturbative part of the radiative corrections to pion and kaon decays given by the  $\gamma W$ -box are robust. The analysis of RC to neutron decays is, as expected, more challenging because of the exponentially decaying signal-to-noise problem and the need to remove possibly large contributions from excited states.

## ACKNOWLEDGMENTS

We thank the MILC Collaboration for providing the HISQ lattices, and Vincenzo Cirigliano and Emanuele Mereghetti for discussions. The calculations used the CHROMA software suite [29]. Simulations were carried out at (i) the NERSC supported by DOE under Contract No. DE-AC02-05CH11231, (ii) the Oak Ridge Leadership Computing Facility, which is a DOE Office of Science User Facility supported under Award No. DE-AC05-00OR22725 and was awarded through the INCITE program project HEP133, (iii) the USQCD Collaboration resources funded by DOE HEP, and (iv) Institutional Computing at Los Alamos National Laboratory. This work was supported by LANL LDRD program and T. B. and R. G. were also supported by the DOE HEP under Contract No. DE-AC52-06NA25396.

- 
- [1] R. L. Workman *et al.* (Particle Data Group), Review of particle physics, *Prog. Theor. Exp. Phys.* **2022**, 083C01 (2022).
  - [2] C.-Y. Seng, M. Gorchtein, H. H. Patel, and M. J. Ramsey-Musolf, Reduced Hadronic Uncertainty in the Determination of  $V_{ud}$ , *Phys. Rev. Lett.* **121**, 241804 (2018).
  - [3] C. Y. Seng, M. Gorchtein, and M. J. Ramsey-Musolf, Dispersive evaluation of the inner radiative correction in neutron and nuclear  $\beta$  decay, *Phys. Rev. D* **100**, 013001 (2019).
  - [4] A. Czarnecki, W. J. Marciano, and A. Sirlin, Radiative corrections to neutron and nuclear beta decays revisited, *Phys. Rev. D* **100**, 073008 (2019).
  - [5] J. C. Hardy and I. S. Towner, Superallowed  $0^+ \rightarrow 0^+$  nuclear  $\beta$  decays: 2020 critical survey, with implications for  $V_{ud}$  and CKM unitarity, *Phys. Rev. C* **102**, 045501 (2020).
  - [6] Y. Aoki *et al.* (Flavour Lattice Averaging Group (FLAG) Collaboration), FLAG review 2021, *Eur. Phys. J. C* **82**, 869 (2022).
  - [7] F. M. Gonzalez *et al.* (UCN $\tau$  Collaboration), Improved Neutron Lifetime Measurement with UCN $\tau$ , *Phys. Rev. Lett.* **127**, 162501 (2021).
  - [8] J. C. Hardy and I. S. Towner, Superallowed  $0^+ \rightarrow 0^+$  beta-decay from  $T_z = -1$  sd-shell nuclei, *J. Phys. Conf. Ser.* **387**, 012006 (2012).
  - [9] A. Sirlin, Current algebra formulation of radiative corrections in gauge theories and the universality of the weak interactions, *Rev. Mod. Phys.* **50**, 573 (1978); **50**, 905(E) (1978).
  - [10] X. Feng, M. Gorchtein, L.-C. Jin, P.-X. Ma, and C.-Y. Seng, First-Principles Calculation of Electroweak Box Diagrams from Lattice QCD, *Phys. Rev. Lett.* **124**, 192002 (2020).
  - [11] P.-X. Ma, X. Feng, M. Gorchtein, L.-C. Jin, and C.-Y. Seng, Lattice QCD calculation of the electroweak box diagrams

- for the kaon semileptonic decays, *Phys. Rev. D* **103**, 114503 (2021).
- [12] A. Czarnecki, W.J. Marciano, and A. Sirlin, Neutron Lifetime and Axial Coupling Connection, *Phys. Rev. Lett.* **120**, 202002 (2018).
- [13] V. Cirigliano, M. Knecht, H. Neufeld, and H. Pichl, The Pionic beta decay in chiral perturbation theory, *Eur. Phys. J. C* **27**, 255 (2003).
- [14] D. Poganic *et al.*, Precise Measurement of the  $\pi^+ \rightarrow \pi^0 e^+ \nu$  Branching Ratio, *Phys. Rev. Lett.* **93**, 181803 (2004).
- [15] A. Czarnecki, W. J. Marciano, and A. Sirlin, Pion beta decay and Cabibbo-Kobayashi-Maskawa unitarity, *Phys. Rev. D* **101**, 091301 (2020).
- [16] W. Altmannshofer *et al.* (PIONEER Collaboration), PIONEER: Studies of rare pion decays, [arXiv:2203.01981](https://arxiv.org/abs/2203.01981).
- [17] Y. Aoki *et al.* (Flavour Lattice Averaging Group (FLAG) Collaboration), FLAG review 2021, *Eur. Phys. J. C* **82**, 869 (2022).
- [18] C.-Y. Seng, D. Galviz, W. J. Marciano, and U.-G. Meißner, Update on  $|V_{us}|$  and  $|V_{us}/V_{ud}|$  from semileptonic kaon and pion decays, *Phys. Rev. D* **105**, 013005 (2022).
- [19] A. Bazavov *et al.* (MILC Collaboration), Lattice QCD ensembles with four flavors of highly improved staggered quarks, *Phys. Rev. D* **87**, 054505 (2013).
- [20] A. Bazavov *et al.* (MILC Collaboration), Scaling studies of QCD with the dynamical HISQ action, *Phys. Rev. D* **82**, 074501 (2010).
- [21] C.-Y. Seng, M. Gorchtein, and M.J. Ramsey-Musolf, Dispersive evaluation of the inner radiative correction in neutron and nuclear  $\beta$  decay, *Phys. Rev. D* **100**, 013001 (2019).
- [22] R. Gupta, Y.-C. Jang, B. Yoon, H.-W. Lin, V. Cirigliano, and T. Bhattacharya, Isovector charges of the nucleon from  $2 + 1 + 1$ -flavor lattice QCD, *Phys. Rev. D* **98**, 034503 (2018).
- [23] A. Deur, S. J. Brodsky, and G. F. de Teramond, The QCD running coupling, *Nucl. Phys.* **B90**, 1 (2016).
- [24] C. Patrignani *et al.* (Particle Data Group), Review of particle physics, *Chin. Phys. C* **40**, 100001 (2016).
- [25] S. Park, R. Gupta, B. Yoon, S. Mondal, T. Bhattacharya, Y.-C. Jang, B. Joó, and F. Winter (Nucleon Matrix Elements (NME) Collaboration), Precision nucleon charges and form factors using  $(2 + 1)$ -flavor lattice QCD, *Phys. Rev. D* **105**, 054505 (2022).
- [26] P. Virtanen *et al.* (SciPy 1.0 Contributors), SciPy 1.0: Fundamental algorithms for scientific computing in Python, *Nat. Methods* **17**, 261 (2020).
- [27] S. A. Larin and J. A. M. Vermaseren, The  $\alpha_s^{*3}$  corrections to the Bjorken sum rule for polarized electroproduction and to the Gross-Llewellyn Smith sum rule, *Phys. Lett. B* **259**, 345 (1991).
- [28] P. A. Baikov, K. G. Chetyrkin, and J. H. Kuhn, Adler Function, Bjorken Sum Rule, and the Crewther Relation to Order  $\alpha_s^4$  in a General Gauge Theory, *Phys. Rev. Lett.* **104**, 132004 (2010).
- [29] R. G. Edwards and B. Joo (SciDAC Collaboration, LHPC Collaboration, UKQCD Collaboration), The Chroma software system for lattice QCD, *Nucl. Phys.* **B140**, 832 (2005).